Investigation of Measurement Errors in Doppler Global Velocimetry

James F. Meyers

Joseph W. Lee

NASA Langley Research Center

Hampton, Virginia 23681-2199 USA

SAE World Aviation Congress and Exposition
Paper 1999-01-5599
San Francisco, California
October 19-21, 1999

1999-01-5599

Investigation of Measurement Errors in Doppler Global Velocimetry

James F. Meyers and Joseph W. Lee
NASA Langley Research Center

ABSTRACT

While the initial development phase of Doppler Global Velocimetry (DGV) has been successfully completed, there remains a critical next phase to be conducted, namely the determination of an error budget to provide quantitative bounds for measurements obtained by this technology. This paper describes a laboratory investigation that consisted of a detailed interrogation of potential error sources to determine their contribution to the overall DGV error budget. A few sources of error were obvious; e.g., Iodine vapor absorption lines, optical systems, and camera characteristics. However, additional non-obvious sources were also discovered; e.g., laser frequency and single-frequency stability, media scattering characteristics, and interference fringes. This paper describes each identified error source, its effect on the overall error budget, and where possible, corrective procedures to reduce or eliminate its effect.

INTRODUCTION

The basis of Doppler Global Velocimetry (DGV) is straightforward: Use the absorption characteristics of Iodine vapor as an optical frequency discriminator to measure the Doppler shift of scattered light from particles passing through a laser light sheet. This direct measure of the scattered light optical frequency depends on physics and technologies far different from other forms of laser velocimetry. Thus, error analyses developed to predict classic laser velocimetry measurement accuracies are inappropriate for DGV. New techniques must be developed, based on the subtle characteristics of the technology, to first identify potential error sources and then establish their effect on the overall DGV error budget.

The interaction of technologies on system characteristics will be illustrated by tracing fundamental processes used in DGV. These processes include the Iodine vapor absorption line calibration, the normalization of the signal image by the reference image, and the conversion from the measured velocity components into standard orthogonal components. As each process is investigated, potential error sources will be identified and their impact on the total measurement error assessed. If the assessment indicates that the error source can be reduced or even eliminated, procedures developed to accomplish the reduction will be described.

DOPPLER GLOBAL VELOCIMETRY – THE BASICS

Doppler Global Velocimetry is a classic example of an advancement in one technology being spun-off from technologies that are routine in another area. The optical absorption characteristics of Iodine vapor are routinely used in laser spectroscopy to stabilize Argon ion lasers to produce a fixed optical frequency in the laser output beam. The edge of the absorption line, Figure 1, acts as an optical frequency discriminator yielding a change in optical transmission through the vapor as a function of optical frequency. In laser spectroscopy a portion of the laser beam is passed through an Iodine vapor cell before impinging on a photo detector. The output from the detector is used as the control signal for heaters on the inter-cavity etalon in the laser. If the photo detector measures a change in laser energy, indicating a change in laser output frequency, the temperature of the etalon (and thus its length) is adjusted to return the laser frequency to the desired value. Komine, Reference 1, adapted this technology in an open loop version to form the basis of Doppler Global Velocimetry.

Komine proposed that by setting the laser frequency to the midpoint along the side of the absorption line, Figure 1, Doppler shifted scattered light would pass through the Iodine vapor with greater (or less, depending on the direction of the Doppler shift) absorption. However, unlike the closed loop version, a change in detected energy was not necessarily caused by a change in optical frequency. Variations in particle number density, particle size distribution, or even the laser energy profile across the beam affects the collected scattered light energy. Thus Komine proposed that the detected energy should be normalized by the total energy of the collected scattered light to remove these dependencies. This would be accomplished by placing a beamsplitter in front of the Iodine vapor cell to direct a portion of the collected light to a second

detector, and dividing the measured signal energy by this *reference* energy value.

The implementation of this technology uncovered characteristics that would make Doppler Global Velocimetry a uniquely capable flow diagnostic measurement system. Unlike other laser velocimetry techniques, optically resolving individual seeding particles was not necessary since the velocity measurement was based on the amount of collected scattered light absorbed by the Iodine vapor. Further, the direct measure of optical frequency eliminated the problems of signal interference from multiple scatterers inherent in standard laser velocimetry. These characteristics allowed the laser beam to be expanded into a light sheet, and the energy detectors replaced with Charge Coupled Device (CCD) video cameras, Figure 2. In this configuration, each pixel element of the CCD became, in effect, a single detector measuring light energy originating from the small volume within the light sheet imaged on that pixel. The ratio of the video output signals from the signal and reference cameras yielded images whose amplitude information was directly related to velocity.

Komine, *et al* at the Northrop Research and Technology Center, Reference 2, first demonstrated these concepts in the laboratory. Further development at the NASA Langley Research Center resulted in the first wind tunnel measurements, References 3 and 4. Additional studies at Northrop, under contract to NASA, found that a pulsed, injection seeded, frequency doubled Nd:YAG laser could be used as the laser source to obtain instantaneous velocity flow field mappings, Reference 5. The current configuration used at Langley consists of a pulsed single-frequency, frequency-doubled Nd:YAG laser along with three optical receiver systems to obtain instantaneous three-component flow velocity maps of the measurement plane.

A laboratory investigation of the basic technology utilized in Doppler Global Velocimetry was conducted using a single component version set to measure horizontal velocity. A pulsed single-frequency, frequency-doubled Nd:YAG laser provided the illumination. This effort used a rotating wheel to provide a velocity standard with a linear profile. The wheel was illuminated with a cone of laser light and the optical receiver system aligned to measure the horizontal component of velocity, 42.1-degrees out of the plane defined by the rotating wheel. The laboratory configuration is shown in Figures 3 and 4, and the optical receiver system is shown in Figure 5. A second optical receiver system was used as the Laser Frequency Monitor (LFM), Figure 3, to simultaneously measure the laser output frequency when the wheel data images were acquired.

OPTICAL FREQUENCY MEASUREMENT UNCERTAINTIES

Since Iodine vapor serves as the primary sensor in DGV, this was an obvious area to investigate for sources of measurement uncertainty. The absorption line transfer function, Figure 1, is a measure of the relationship between light absorption and optical frequency. The ability to determine this relationship depends on the measurement precision of the absorption level for a given optical frequency, and the capability to determine that frequency.

The absorption line transfer function is measured by illuminating translucent vellum placed in the light sheet plane with laser light and acquiring signal and reference images by each optical receiver system (one system for the present study, and three for wind tunnel testing). Signal and reference images are also acquired by the laser frequency monitoring system. Thus the two (or four) Iodine vapor cells are calibrated simultaneously. The fidelity of these calibrations however, is directly related to the amplitude measurement precision of the video cameras.

Image amplitude measurement precision is dependent on the linearity and signal-to-noise characteristics of each CCD video camera and its acquisition frame grabber. The CCD array serves as the energy sensor to convert light energy patterns into electronic charge distributions. The charge stream is then transferred to the video analog-to-digital converter, or frame grabber, for digitization. The CCD sensor and frame grabber can be physically separate, or contained within the same unit, e.g., a digital video camera. Since the Iodine vapor absorption line calibration and all DGV data acquisition begins with the sensing of light energy by video cameras, the investigation of measurement uncertainty began by characterizing the cameras.

CAMERA SIGNAL-TO-NOISE RATIO

Video camera manufacturers typically do not provide linearity specifications and are inconsistent in their signal-to-noise specifications. Normally signal-to-noise is related to the variation of electronic output noise as a function of light intensity level. Thus the expected quoted value would be related to the noise level found at the maximum light energy just below CCD saturation. Although this is the case for many manufacturers, a few base their values on the signal level at saturation and the noise level established by the dark current. Other manufacturers, especially digital camera manufacturers, base their signal-to-noise ratios on the quantizing error of the lowest significant bit regardless of the actual noise. Without confirmation by the user, the quoted signal-to-noise ratios should only be accepted as comparison guides between cameras from the same manufacturer.

Another definition of signal-to-noise, and the one used in this investigation, is based on the consistency of the measured image intensity for each pixel over a large number of images. This measure of performance stability can be more important for instrumentation applications than the pixel-to-pixel noise found in a single image. By viewing a uniformly illuminated

transparency containing a series of increasingly optically dense gray scale boxes, Figure 6, the camera consistency could be determined. Each camera / frame grabber acquired 100 images of the back-illuminated transparency. A 10-x 10-pixel subregion was selected from each of the 10 gray scale portions of the image. The mean and standard deviation were calculated for each pixel within the subregion throughout the 100 images. Each mean value represented the signal, and the standard deviation represented the noise. The resulting 100 signal-to-noise ratios were averaged to obtain a measure of the camera signal-to-noise for that illumination level. The camera / frame grabber signal-to-noise profile was obtained by plotting the 10 averaged signal-to-noise ratios. The resulting signal-to-noise ratio profiles for several camera / frame grabber combinations are shown in Figure 7. The current DGV configuration uses an industry standard RS-170 camera with a 10-bit frame grabber that produces an effective 8.5 bits of resolution. This yields an uncertainty of ±3 levels out of the 1024 level full-scale capability.

OPTICAL FREQUENCY TUNING

With the amplitude measurement precision defined, the analysis continued by determining the accuracy of the laser frequency as it is tuned through the Iodine vapor absorption line during calibration. The fidelity of the calibration is dependent on the laser frequency bandwidth and the tuning increments. A single-frequency Argon ion laser operating at 514.5 nm has a bandwidth of approximately 10 MHz. This narrow bandwidth minimizes averaging of the absorption line characteristics to the point where even the minor hyperfine structure can be observed. A single-frequency, frequency-doubled Nd:YAG laser operating at 532.0 nm has a bandwidth of approximately 100 MHz. This wider bandwidth averages out the hyperfine structure and reduces the useful measurement range since the optical frequency spectrum will be modified if the bandwidth overlaps the bends in the Iodine absorption line.

The two lasers are frequency tuned in totally different ways. The Argon ion laser is tuned by adjusting the effective thickness of the inter-cavity etalon. Large frequency adjustments are accomplished by tilting the etalon to *mode hop* the optical frequency to the next longitudinal mode of the laser cavity. This results in a frequency shift of approximately 129 MHz in a nominally 5 W laser, and approximately 72 MHz for the longer cavity length 15 W laser. Changing the etalon temperature to thermally expand, or contract, the etalon thickness provides smaller adjustments. Unfortunately, temperature tuning is a very slow process and does not have sufficient dynamic range to allow calibration of the absorption line.

The Nd:YAG laser operates in single frequency using a stable laser diode to inject seed photons into the Nd:YAG laser cavity. By adjusting the drive voltage to the thermal electric cooler, the diode junction temperature changes in the injection seed laser, which in turn alters the output laser frequency. When the frequency of the seed laser beam changes, the Nd:YAG laser frequency adjusts to match. An electronic feedback control system optimizes the laser cavity length using piezoelectric transducers to bring the cavity into resonance with the new frequency. This technique provides continuous tuning of the optical frequency with a dynamic range of approximately 30 GHz.

IODINE VAPOR CELL CALIBRATION

With the ability to tune the optical frequency of the laser, the calibration of the two (or four) Iodine vapor cells is straightforward. Adjust the laser frequency to a point just outside the absorption line, acquire 10 image sets, change the laser frequency by a known amount, wait until the laser reaches stability, and acquire the next 10 image sets. This process is repeated until the absorption line is characterized. Unfortunately this calibration procedure has two flaws: the assumptions that the frequency increment between measurement points is known and constant, and that the time needed for the laser to reach stability is constant.

These flaws are minimized when an Argon ion laser is used. The frequency increment is based on the length of the laser resonator cavity and is determined theoretically. Since the laser frequency is adjusted by *mode hopping* the laser by tilting the etalon, the time to reach stability is short. However, this technique only provides a few data points along the edge of the absorption line, which lessens the fidelity of the calibration. The Argon ion laser also has the tendency to drift in optical frequency, which causes the output to oscillate between two adjacent longitudinal modes. Thus the laser output must be monitored using a confocal interferometer to insure operation in single longitudinal mode.

The Nd:YAG laser provides the capability to adjust the laser frequency continuously by temperature tuning the injection seed laser. When the laser frequency is changed, a period of time is necessary for the seed laser temperature and thus the output optical frequency to stabilize. This sensitivity to temperature causes a long-term frequency drift with random shot-to-shot frequency variations. With these changes in laser frequency, single frequency operation can not be adequately maintained. A flat-plate interferometer is needed to monitor each pulse to determine if individual pulses are single frequency and usable for DGV measurements.

The Iodine vapor absorption line was calibrated in the laboratory using the Nd:YAG laser to illuminate the vellum target placed in front of the wheel, Figure 3. The laser frequency was adjusted using the manufacturer-supplied injection seed laser calibration of 1 V/GHz. The laser was tuned to a point outside the absorption line and allowed to stabilize for 40 seconds. Ten data images were then acquired. The laser frequency was changed by 20 MHz, the system was allowed to stabilize

for 40 seconds, and then ten data images were acquired. This process was repeated until the absorption line was defined, Figure 8. The vellum target was removed, the laser set to approximately the mid-point of the absorption line, and the wheel spun to 3,000 rpm. Thirty data images were acquired, processed, averaged and interrogated to determine the normalized signal level along the vertical diameter. The resulting signal level was found to be linear, Figure 9. This test was repeated on successive days to determine if the data remained linear and had the same slope. A least square linear fit was performed for each set of data and overlaid with the original Iodine calibration in Figure 8. Expanding the plots, Figure 10, clearly shows that the slope of the wheel data did not match the calibration. Further, the calibration was not linear, Figure 10, or repeatable, Figure 11.

The difference in slope between the Iodine absorption line calibration and the spinning wheel data indicated that the manufacturer-supplied seed laser calibration of 1 V/GHz was incorrect. Since it was not possible to rotate the wheel at sufficient speeds to obtain the full absorption line calibration, a comparison of line shapes with theory may provide the correct calibration. The line shape for two adjacent absorption lines was calculated to obtain two known optical frequency locations, represented by the center of each line. The laser was adjusted to locate these lines within its frequency scan range, and an Iodine absorption line calibration performed. The horizontal axis of the calibration was adjusted until it overlaid the theoretical predictions, Figure 12. The seed laser calibration was thus found to be 0.549 V/GHz. Additionally, a scanning confocal interferometer was used to confirm these results. A five-point linear fit over the injection seed laser tuning range yielded a conversion factor of 0.559 V/GHz.

The non-linearities and lack of repeatability in the calibration data could be observed in more detail by plotting the calibration values for each data block, Figures 13 and 14. The data inconsistencies in each data block and large variations between data blocks indicate that the laser had not reached stability when the data was acquired. A feedback network based on a flat-plate interferometer must therefore be used to allow data acquisition only when frequency stability and single-frequency operations occur. The flat-plate interferometer will provide optical quality measurements of each Nd:YAG laser pulse that would be interrogated by the computer to determine when the laser has stabilized.

IODINE VAPOR CELL – TEMPERATURE DEPENDENCE

Now that procedures were developed to conduct the calibration of the Iodine vapor absorption line, the characteristics of the Iodine vapor were investigated. The Iodine vapor absorption line shape is dependent on the vapor pressure within the cell. As the vapor pressure increases, more molecules sublime from crystalline Iodine into the vapor state. The increased number of vapor molecules will enhance the capability of the vapor to absorb light. From a spectral viewpoint, the absorption at the center of the line will increase until all light at that optical frequency is absorbed. The width of the absorption line will also grow, and the optical density for frequencies outside the line will increase until the vapor is totally opaque to all light. However, as the line width enlarges with increased molecular density, the slope remains essentially the same.

Assuming crystalline Iodine is present in the cell, the vapor pressure is determined by the temperature of the coldest part of the cell. Typically, a glass stem or *cold finger* is attached to the cell body and immersed in a temperature controlled water bath. The cell body is heated to at least 10° C above the bath temperature to keep the vapor pressure stabilized. If large cells are used, the body temperature should be set even higher to insure that all crystalline Iodine is in the cold finger and not plating the windows.

Since water bath heaters were not practical for wind tunnel applications, an oxygen-free copper jacket was placed about the cold finger and heated with band heaters. A heat-transfer wire was attached between the end of the cold finger and the optics bench to provide a positive heat transfer from the heaters to the cell to the bench. A thermocouple was attached to the cold finger to provide a control signal to the heater control electronics. This system was capable of maintaining a constant temperature within ±0.1° C. A similar approach was used to heat the cell body. The cell, copper jackets, and heaters were encased in an insulated container, Figure 5.

The heated Iodine vapor cell worked well in the laboratory yielding a velocity uncertainty of ±3 m/s based on a temperature uncertainty of ±0.1° C. When the system was installed in the 14-by 22-Foot Subsonic Tunnel, the heating system was incapable of maintaining the calibration temperature as the ambient temperature fell to 5° C. Thus the calibration of the Iodine vapor absorption line was no longer applicable. Further, the vapor temperature varied continuously during testing as the heating system attempted to track the changes in the ambient temperature. This prohibited the possibility of calibrating the absorption line following the test at the test temperature.

The dependence of the absorption line shape on temperature may be eliminated if all of the Iodine in the cell is maintained in the vapor state. The Iodine vapor cells were returned to the manufacturer to be filled with Iodine vapor at a pressure matching the vapor pressure at 45° C. Thus the absorption line shape should be constant for all temperatures greater than 45° C. The calibration of this *vapor limited* cell at 35° C, 40° C, and 60° C are compared with the calibration at 50° C in Figures 15 – 17 respectively. The results in Figure 15 indicate that crystalline Iodine was present in the cell since the absorption line was narrower than the 50° C calibration. The matching calibrations in Figure 16

indicate that all Iodine had vaporized at 40° C. Finally, the matching calibrations in Figure 17 verify that the line shape remains stable for vapor temperatures greater than 40° C. Operating the Iodine vapor cell at a vapor temperature of 55° C would provide a safety margin should the heaters fail to maintain the cell temperature when the ambient temperature falls to low levels. Thus the use of vapor limited cells eliminates the dependence of absorption line shape on temperature, and even eliminates the ±3 m/s uncertainty found in the laboratory.

RECEIVER CAMERA REGISTRATION

DGV measures the flow velocity field by imaging the laser light sheet on a CCD array. Each CCD element or pixel is thus collecting scattered light from a specific volume within the light sheet. The light sheet area imaged on the pixel, as projected through the light sheet thickness, defines this volume. To properly eliminate dependency on particle number density, particle size distribution, and spatial variations in laser illumination, the volume viewed by a pixel in the signal camera must also be viewed by the corresponding pixel in the reference camera. Thus great care must be used to insure that both cameras are in perfect alignment including matching focal distances.

While challenging, aligning two video cameras to view the same scene along a common optical axis should be possible. The results reported in References 1 – 3 testify to the possibility of obtaining velocity measurements in this manner. Unfortunately, perspective distortion of the light sheet will be different for each receiver in a three-component configuration. It is impossible to obtain pixel-by-pixel overlap among corresponding pixels in the six viewing cameras. Thus a method was developed to remove perspective distortions from the camera images to obtain the overlap needed to compute the orthogonal velocity components.

A laboratory investigation was conducted to determine the effectiveness of careful alignment of the optical receiver system. A test target, Figure 18, was placed in the laser light sheet plane and viewed by the optical receiver system. The signal and reference camera video signals were input to a custom electronics circuit that normalized the signal camera output by the reference camera output. If the alignment of the two cameras was perfect, the variation in light intensity (dots) should disappear leaving a flat gray image of constant amplitude. Unfortunately, the edges of the dots on the test target were clearly visible, with overall patterns indicative of differences in the optical characteristics between the signal and reference optical paths, Figure 19. Adjusting camera position, pan, tilt, and magnification improved the normalized image, but perfect alignment was never achieved. The inability to obtain the proper alignment was traced to minor imperfections in the optical receiver elements.

The inclusion of minor optical distortions in the signal and/or reference images prohibited the use of commercial dewarping software found to be capable of only removing perspective distortions. Although not usable, the commercial image processing software provided insight into a potential solution. Instead of dewarping the entire image with a single equation, the image was subdivided into numerous smaller images whose characteristics could better be approximated by linear dewarping. Each dot serves as a corner of a sub-image that can be dewarped using bilinear warping procedures, References 4 and 6. In practice, a grid of 20 by 20 sections, defined by the dot centroids in the test target, appeared to yield sufficient correction. Dewarping Figure 18 with this method yielded Figure 20. The improvement in image alignment can be seen in Figure 21 when the signal image was dewarped and normalized by the dewarped reference image.

Placing three optical receiver systems about the test target continued the laboratory investigation. The three systems were placed 30-degrees out of plane, on the left, right, and above the test target. The three reference camera images are shown in Figure 22 along with their dewarped versions. A wheel was then placed in the test target plane. The wheel was rotated at 3,000 rpm and 30 sets of data images acquired. The resulting velocity maps for components A, B, and C are shown in Figure 23. The standard orthogonal velocity components U, V, and W were computed for corresponding pixels within the A, B, and C data images, yielding the computed velocity maps shown in Figure 23.

The velocity data presented in Figure 23 indicates that the dewarping procedures were sufficiently accurate to determine the orthogonal velocity components from the dewarped A-, B-, and C-component maps. This does not, however, give an indication as to the measure of spatial uncertainty in the dewarping process. If an analytical function were chosen to simulate a transition from black to white intensity levels, the resulting characteristics for misaligned signal and reference images could be categorized. By comparing the characteristics of the edge of a rotating wheel in the dewarped DGV velocity data with the theoretical categorizations, the actual image misalignment could be determined. A hyperbolic tangent (*tanh*) function was chosen to provide an analytic transition from black to white intensity levels:

$$SIG = 150 (\tanh(x) + 2), \quad -2 \le x \le 2$$

$$REF = 300 (\tanh(x) + 2), \quad -2 \le x \le 2$$

where SIG and REF are the signal and reference intensities respectively and x is distance. The slope could be adjusted from a gradual transition to a step function by adjusting the number of pixels mapped into the function limits of $-2 \le x \le 2$. For example, a mapping from –5 pixels to 5 pixels of the signal and reference intensities yielded the transitions shown in Figure 24. The signal intensity was normalized by the reference intensity and multiplied by 500 to yield the error function. When the two functions were aligned precisely, the

normalized function was a constant level of 250 regardless of the transition slope. When the signal image was misaligned, an impulse function occurred in the center of the transition. A 0.2-pixel misalignment of the signal position resulted in the error function shown in Figure 24. If the signal was misaligned to the right, as

tanh (x)	levels/pixel	Signal/Reference image misalignment				
-2 < x < 2		0.01 pixels	0.05 pixels	0.1 pixels	0.2 pixels	0.3 pixels
maps from		Edge impulse width (pixels)				
-250->250 pixels	2.32	-	-	-	-	-
-100->100 pixels	5.64	-	-	-	-	74
-50->50 pixels	11.15	-	-	14	46	61
-25->25 pixels	18.77	-	7	24	34	40
-10->10 pixels	48.23	-	11	16	18	21
-5->5 pixels	79.00	1	8	9	11	12
-2.5->2.5 pixels	150.50	1	4	6	6	8
-1->1 pixels	177.70	1	3	3	3	3
-0.5->0.5 pixels	299.50	1	1	1	2	2

Table 1.- Impulse characteristics for black-to-white intensity transitions as the signal image is misaligned with the reference image.

was the case in Figure 24, the impulse was positive. If misaligned to the left, the impulse would be negative. Increasing the sharpness increased the impulse amplitude while decreasing its width. The results of several combinations of function slope and signal misalignment are given in Table 1.

The normalized signal amplitude profile along the vertical diameter of the rotating wheel is shown in Figure 25. Close inspection of the vertical profile indicates that the left edge (top of wheel) had a 5-pixel roll off, and the right edge had a 5-pixel impulse. This indicates a misalignment of the signal image toward the top of the wheel. The measurement of the black-to-white edge function for each camera was determined to be approximately 5 pixels, as measured from 10-percent to 90-percent of the full-scale amplitude. These results indicate that the image overlap uncertainty was less than 0.1 pixels based on the simulated results given in Table 1.

The implications of these results on wind tunnel measurements are described as follows. If the smoke cloud has a uniform number density and the velocity field is flat, an alignment to within 0.1 pixels is sufficient to reduce spatially dependent uncertainties to negligible levels. Otherwise, gradients in number density will result in the impulse characteristics found in Figure 25, even if the velocity field was flat. Since the smoke plume normally moves about during an acquisition sequence, these anomalies will occur randomly with random amplitudes throughout the velocity field as the acquisition sequence progresses. Thus the processing code should include tests to only process areas within the image where the intensity gradients would result in negligible velocity anomalies, thereby eliminating these errors.

IMAGE AMPLITUDE CONSIDERATIONS

Ideally the normalization of the signal image by the reference image would remove collected scattered light intensity dependencies from the data images. Unfortunately, this is not the case. There are several situations where the amplitude of the collected scattered light intensity can induce errors in the velocity measurements. For example, any change in the optical transmission characteristics occurring in either the signal or reference optical path that does not occur in the other generates a measurement error. Additionally, if the scattered light intensity is low, quantizing errors become significant.

When viewing scenes through optical systems, especially when using coherent laser light, there is the potential for spatial variations in the transmission of light reaching the video cameras. For example, the deposit of dirt or seeding particles on the tunnel window may not be uniform, resulting in a variable transmissivity across the window. In this case the normalization process will eliminate the effect of variable transmissivity since it occurs in the common optical path. Effects that could occur in one optical path and not the other include

physical blockages, interference fringes, and scattered light polarization.

Physical blockage of light includes dirt, fingerprints, a film left on the lenses caused by improper cleaning, and non-uniform optical densities in the beamsplitter, mirror, lenses, or the Iodine vapor cell. Sensitivity patterns in the camera CCD have the same effect as dirt on the lens. Blockage-type errors can be eliminated using a flat field correction image. The flat field image is obtained by illuminating a vellum target with laser light set to an optical frequency outside the absorption line and acquiring a block of 20 data images. After normalizing each signal image by its respective reference image, the average normalized data image is computed. Averaging reduces laser speckle noise, CCD pixel sensitivity variations, and charge transfer noise effects on the flat field. The image amplitudes are inverted to produce the flat field correction image. The blockage-type errors in the normalized data images are removed by simply multiplying each image by the correction image. An example flat-field correction image is shown in Figure 26.

When coherent laser light passes through optical systems, reflections from glass surfaces can interact with the incoming light to produce interference fringes. In the DGV optical receiver system, the windows on the Iodine vapor cell are likely candidates for interference fringes since the windows have two parallel surfaces. Example interference fringes caused by the Iodine vapor cell are shown in Figure 27. These fringes affect the measured scattered light intensity in the same manner as the blockage-type error sources and are likewise eliminated by applying the flat field correction image.

The orientation of the collected scattered light polarization affects the normalization process since the beamsplitter is polarization sensitive. This effect can be illustrated by considering the following example. Linearly polarized light scattered from small particles remains polarized. The polarization angle of the scattered light depends on the viewing direction and the effects of Mie scattering. If the optical receiver system is placed along a given scattering angle and the seeding particles are monodisperse (i.e., a narrow size distribution), the scattered light polarization remains constant. However, if the particle size distribution is polydisperse, the polarization angle will vary as described by Mie scattering theory. If the beamsplitter is sensitive to polarization, such as reflecting/ transmitting different ratios for s- and p-type polarizations, the fluctuation in polarization from polydisperse particles will vary the ratio of light passed to the signal and reference cameras respectively. Thus the normalization process will be affected by these changes in polarization. The solution for this source of measurement error consists of installing a non-polarizing beamsplitter and a polaroid filter at the optical entrance to the optical receiver system. The polaroid filter is required because even *non-polarizing* beamsplitters have a non-negligible dependence on polarization.

The remaining amplitude dependent error is the quantizing error obtained when the video analog-to-digital converter digitizes the analog camera signal. Typically this error is the uncertainty of ±1-bit. The error is amplitude dependent when the accuracy is based on a percentage of reading, Figure 28. Since DGV measurements rely on the normalization of the signal image by the reference image, quantizing error is present in both the numerator and denominator, thus increasing the effective quantizing error, Figure 28. It is also affected by the camera signal-to-noise ratio. For example, if the camera signal-to-noise ratio were found to be 45 dB, the amplitude measurement uncertainty would be ±1 part in 178. Since an 8-bit video analog-to-digital converter would yield a quantizing uncertainty of ±1-bit or ±1 part in 256, the camera signal-to-noise ratio and not the converter would control the effective quantizing error. Thus the effective quantizing error is determined from the camera/frame grabber signal-to-noise ratios shown in Figure 7.

OTHER ERROR SOURCES

The effectiveness of the error analysis and the corrective procedures was determined by measuring the velocity distribution of a rotating wheel. After applying the above procedures to the acquired data, the results, shown in Figure 29, indicated a velocity bias error was present in the data. An investigation into the cause of this bias error revealed that there was a difference in the normalized amplitude based on the scattering media. The scattering characteristics of the vellum used as the target during the Iodine vapor absorption line calibration were different from the rotating wheel characteristics. Using the wheel as the flat field calibration target instead of the vellum eliminated this problem, Figure 30. The cause of this effect is not understood at this time, and the investigation continues since it is unknown whether this solution will work with seeding particles.

Additional error sources that are being investigated include uncertainties in determining the geometric locations of the DGV components and laser speckle noise. The geometric uncertainties are determined using standard trigonometric error analyses and result in uncertainties in the conversion of Doppler frequency to velocity. Laser speckle noise affects the image amplitude by superimposing spatially high frequency random noise on the image. The speckle pattern obtained by the signal camera is different from the pattern obtained by the reference camera since speckle noise is dependent on the optical path traversed prior to detection. Thus instead of decreasing the uncertainty, normalization increases the effects of speckle noise on the DGV images. Since speckle noise is spatially random, low-pass filtering techniques can be used to reduce the effects. However, the low-pass filters must maintain high-frequency velocity structures such as shock waves, while reducing the noise. Meyers *et al*, Reference 7, used Median filters, Reference 8, to reduce the influence of speckle noise on the signal and reference images while maintaining the integrity of

velocity structures. The normalized image was also filtered using Median filters to reduce quantizing noise. Smith, Reference 9, used Gaussian filters to perform the same function. While the Median filter maintained the velocity structures better than the Gaussian filter, the Gaussian filter was not nearly as computationally intensive as the Median. Since both filters appear to reduce speckle noise equally, the Gaussian filter approach is recommended unless velocity structures can not be clearly delineated.

SUMMARY

While simple in concept, Doppler Global Velocimetry has proven to be a sophisticated technology. The investigation conducted to determine the contributors to measurement uncertainty found very subtle error sources with few parameters that could be monitored to insure optimal operation. The contributors to measurement uncertainty discussed included laser stability, laser frequency uncertainties, Iodine vapor absorption line characteristics, optical system characteristics, and camera signal-to-noise ratios. This investigation has provided insight into the technology that resulted in the development of operational procedures and data processing techniques that would monitor the condition of the instrument and reduce measurement uncertainty. There remains, however, the transition of these techniques from the laboratory to the wind tunnel. Only then will the error budget of the technique be fully quantified.

REFERENCES

1. Komine, H.: System for Measuring Velocity Field of Fluid Flow Utilizing a Laser -Doppler Spectral Image Converter. US Patent 4,919,536, 1990.
2. Komine, H.; Brosnan, S. J.; Litton, A. B.; and Stappaerts, E. A.: *Real-time Doppler Global Velocimetry.* AIAA 29th Aerospace Sciences Meeting, Reno, NV, paper AIAA 91-0337, January 7-10, 1991.
3. Meyers, J. F.; and Komine, H.: *Doppler Global Velocimetry - A New Way to Look at Velocity.* Laser Anemometry: Advances and Applications, 1991, eds. A. Dybbs & B. Ghorashi, ASME, pp. 289-296, 1991.
4. Meyers, J. F.: *Doppler Global Velocimetry – The Next Generation?.* AIAA 17th Aerospace Ground Testing Conference, Nashville, TN, Paper AIAA 92-3897, July 6-8, 1992.
5. Komine, H.; Brosnan, S. J.; Long, W. H.; and Stappaerts, E. A.: Doppler Global Velocimetry Development of a Flight Research Instrumentation System for Application to Non-intrusive Measurements of the Flow Field. NASA Report CR-191490, 1994.
6. Meyers, J. F.: *Development of Doppler Global Velocimetry for Wind Tunnel Testing.* AIAA 18th Aerospace Ground Testing Conference, Colorado Springs, CO, paper AIAA 94-2582, June 1994.
7. Meyers, J. F.; Lee, J. W.; Fletcher, M. T.; and, South, B. W.: *Hardening Doppler Global Velocimetry Systems for Large Wind Tunnel Applications.* AIAA 20th Advanced Measurement and Ground Testing Technology Conference, Albuquerque, NM, paper AIAA 98-2606, June 15-18, 1998.
8. Astola, J. and Kuosmanen, P.: Fundamentals of Nonlinear Digital Filtering. CRC Press, New York, 1997.
9. Smith, M. W.: *Application of a Planar Doppler Velocimetry System to a High Reynolds Number Compressible Jet.* AIAA 36th Aerospace Sciences Meeting & Exhibit, paper AIAA 98-0428, Reno, NV, January 12-15, 1998.

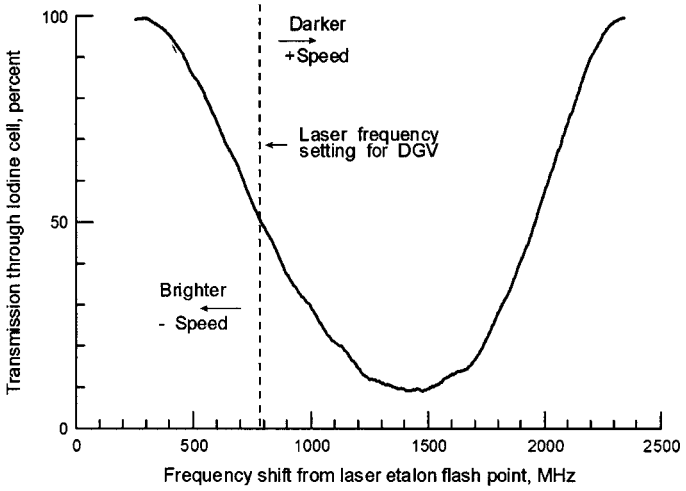

Figure 1.- Transfer function of the Iodine vapor absorption line.

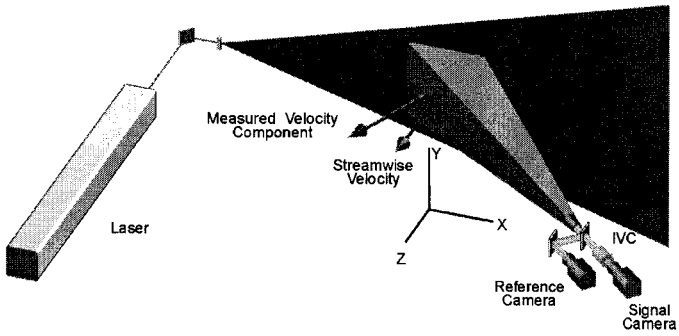

Figure 2.- Single-component Doppler Global Velocimeter configuration.

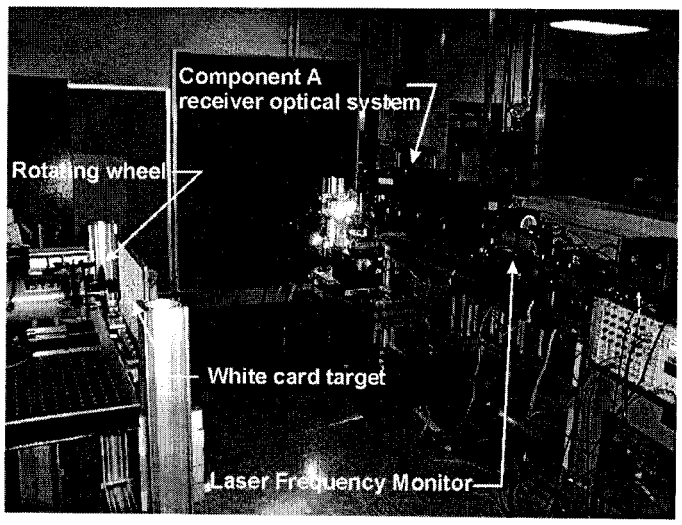

Figure 3.- Doppler Global Velocimetry laboratory.

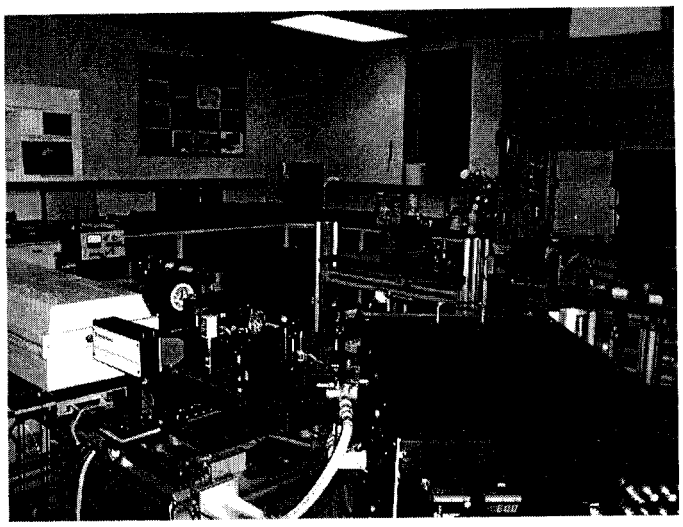

Figure 4.- View of the rotating wheel from above the optical receiver system.

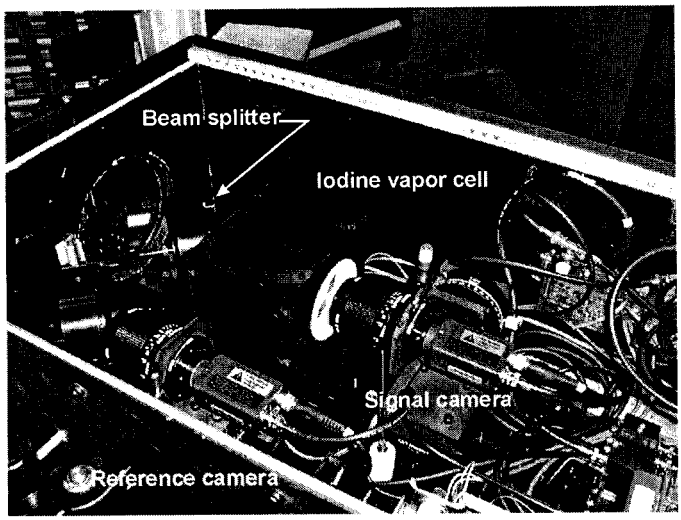

Figure 5.- Doppler Global Velocimeter optical receiver system.

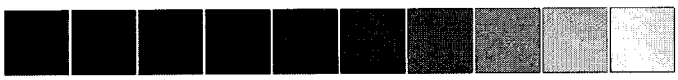

Figure 6.- Video camera calibration target.

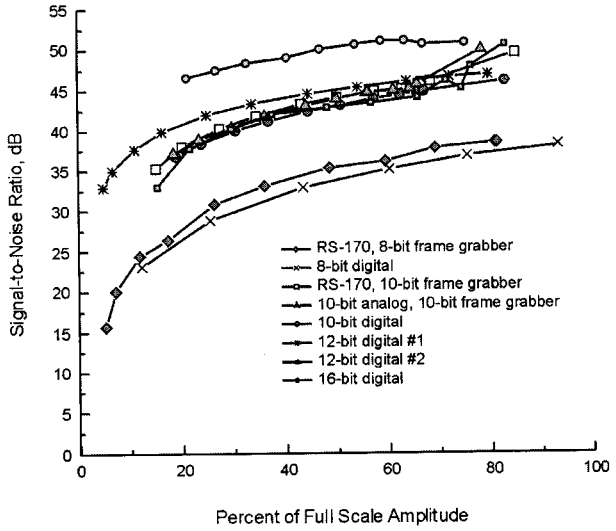

Figure 7.- Camera / frame grabber signal-to-noise response based on statistical noise obtained from 100 acquired images.

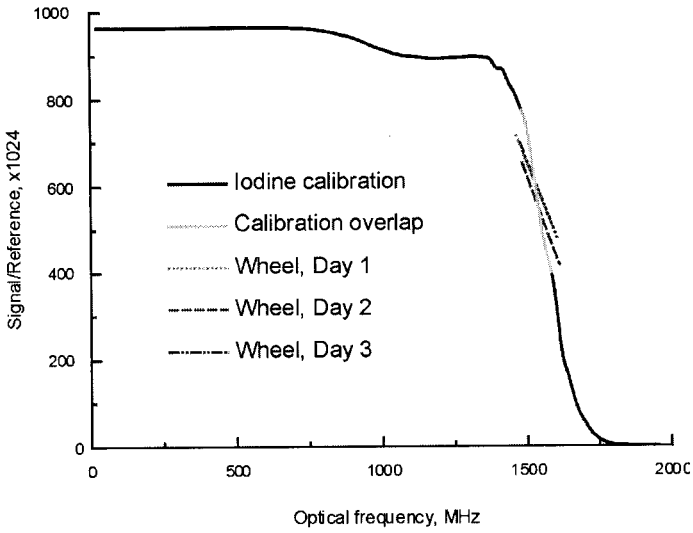

Figure 8.- Superposition of the Doppler shift frequency profiles measured from the rotating wheel on the Iodine vapor absorption line calibration.

Figure 9.- Signal/reference ratio along the vertical diameter of a rotating wheel.

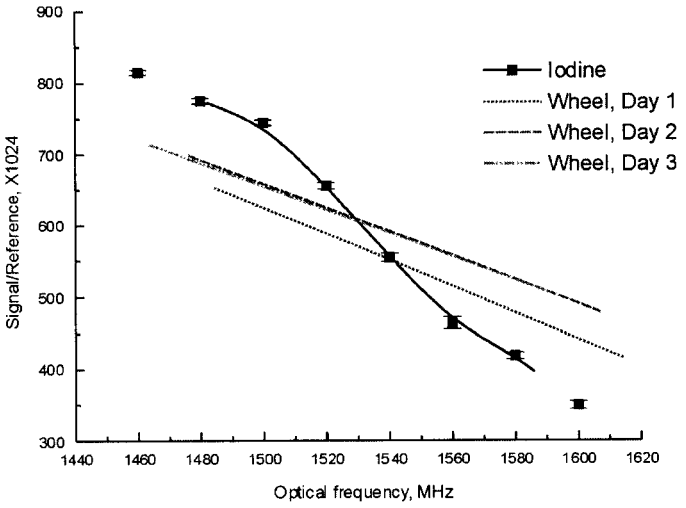

Figure 10.- Expansion of Figure 8 comparing the linear DGV measurements with the non-linear Iodine calibration.

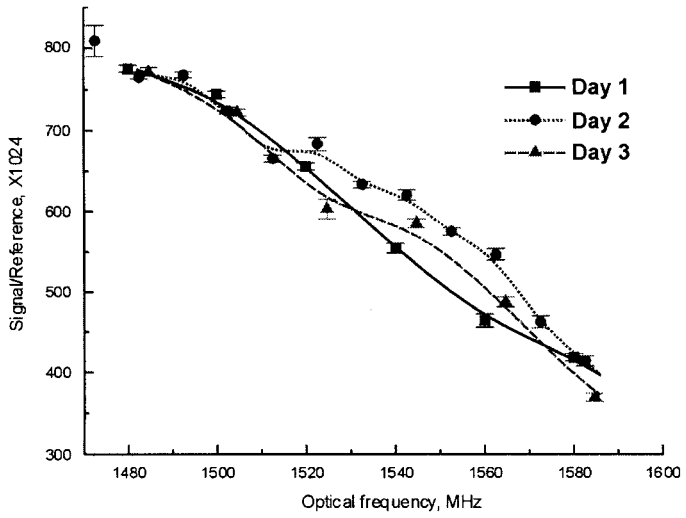

Figure 11.- Comparison of repeated Iodine vapor absorption line calibrations, cell temperature: 50° C.

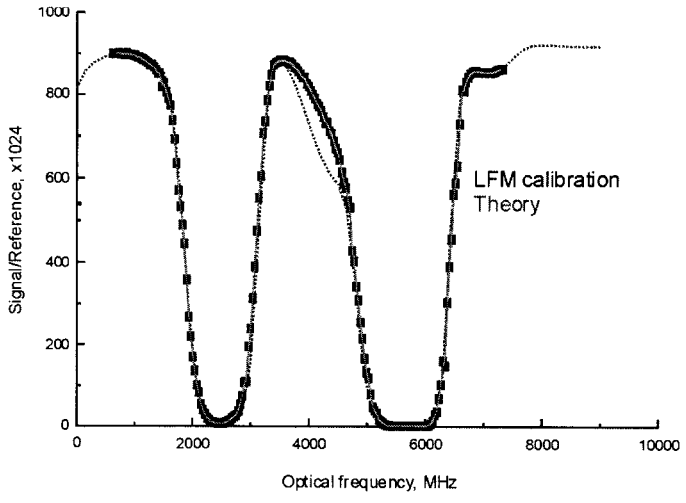

Figure 12.- Comparison of the measured Iodine vapor calibration with a theoretical prediction.

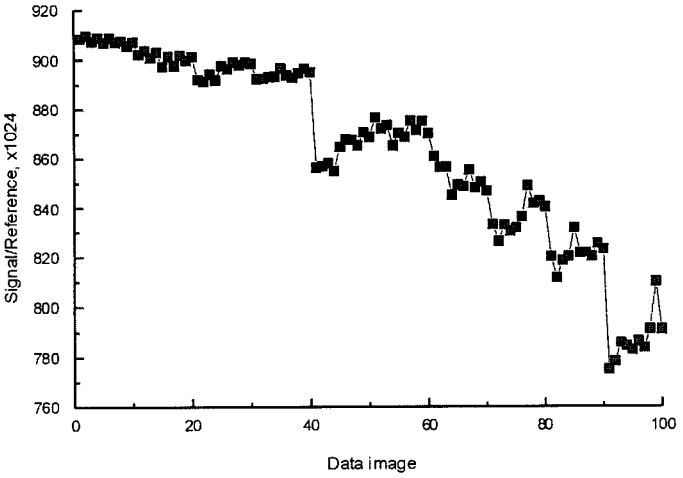

Figure 13.- Iodine vapor absorption line calibration, 10 data points were acquired per laser frequency setting.

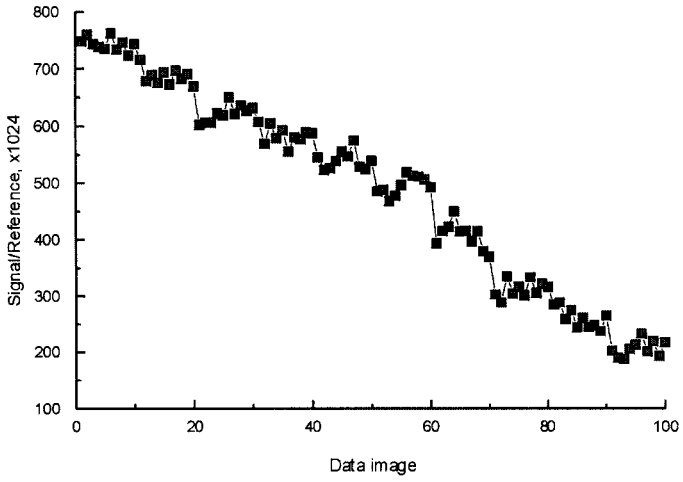

Figure 14.- Iodine vapor absorption line calibration, 10 data points were acquired per laser frequency setting. (Continued)

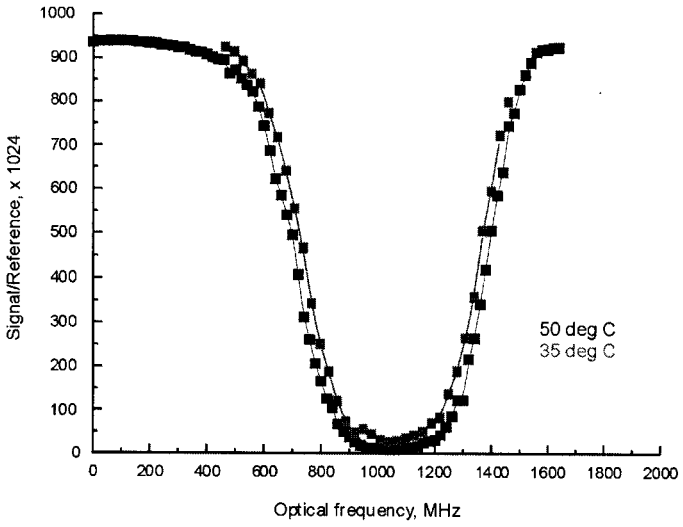

Figure 15.- Comparison of Iodine vapor absorption line calibrations at 35° C and 50° C.

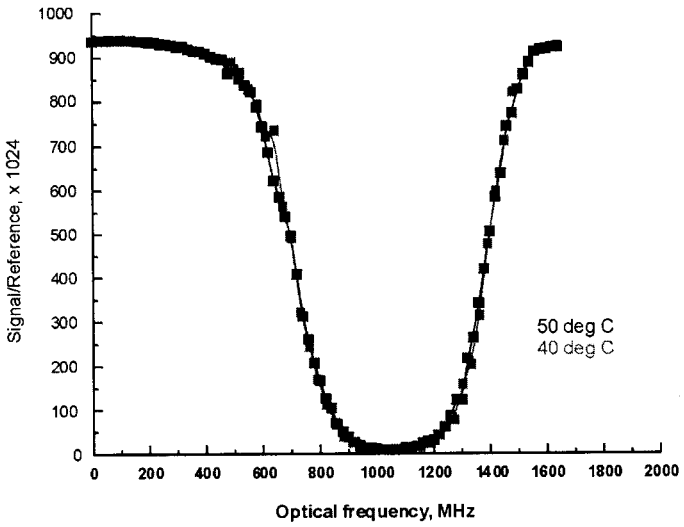

Figure 16.- Comparison of Iodine vapor absorption line calibrations at 40° C and 50° C.

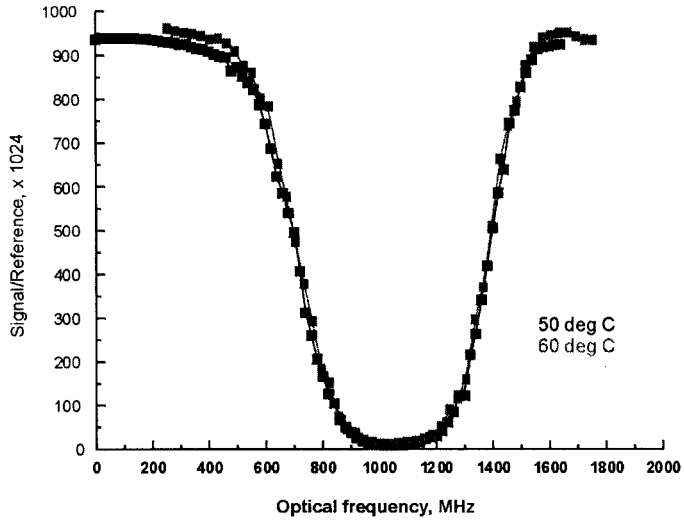

Figure 17.- Comparison of Iodine vapor absorption line calibrations at 60° C and 50° C.

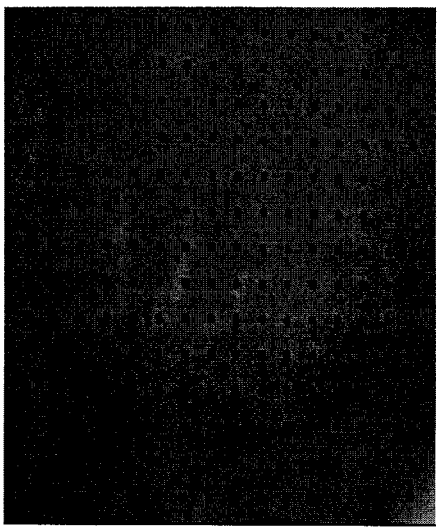

Figure 18.- Camera view of the image alignment target.

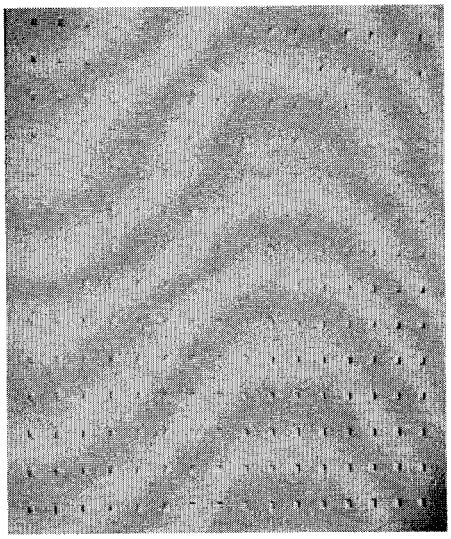

Figure 19.- Signal camera image of the alignment target normalized by the reference camera image.

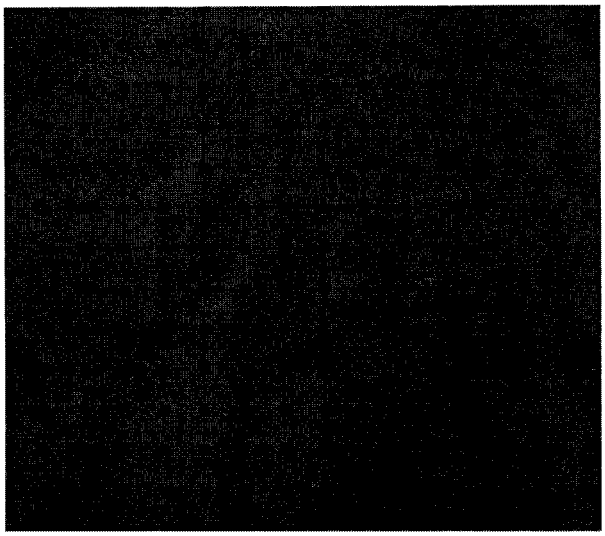

Figure 20.- Dewarped camera view of the image alignment target (from Figure 18).

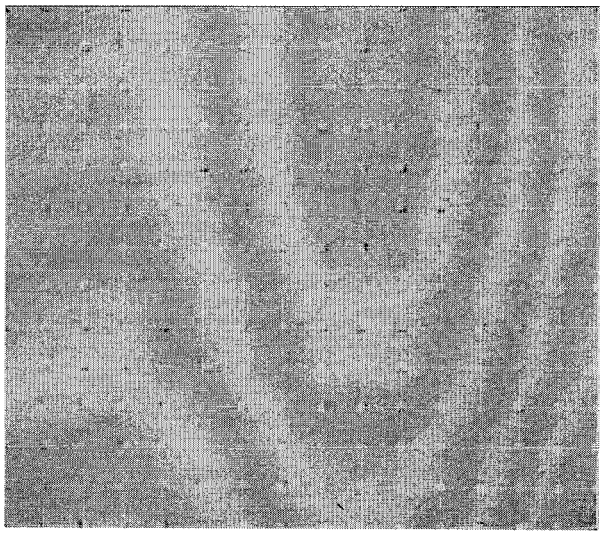

Figure 21.- Dewarped signal camera image of the alignment target normalized by the dewarped reference camera image.

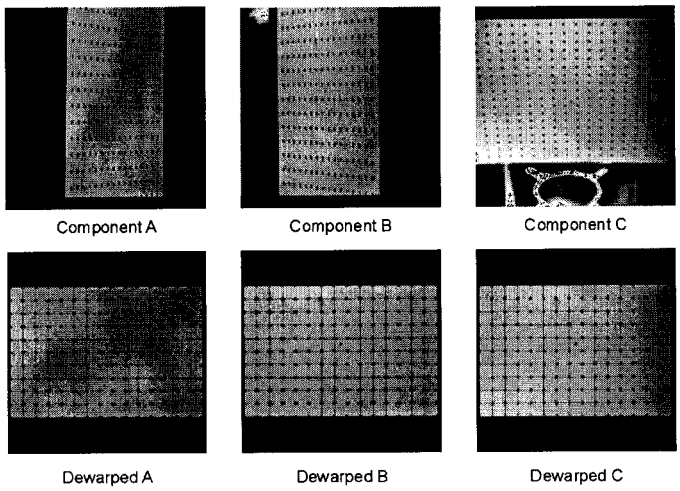

Figure 22.- Views of the image calibration target from the left, right, and above with an inclination angle of 30-degrees from the target plane before and after dewarping.

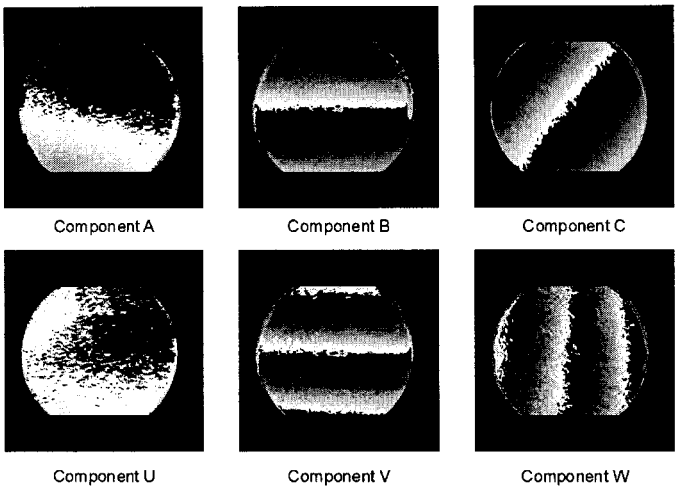

Figure 23.- Three-component velocity measurements of the rotating wheel and the resolved orthogonal velocity maps.

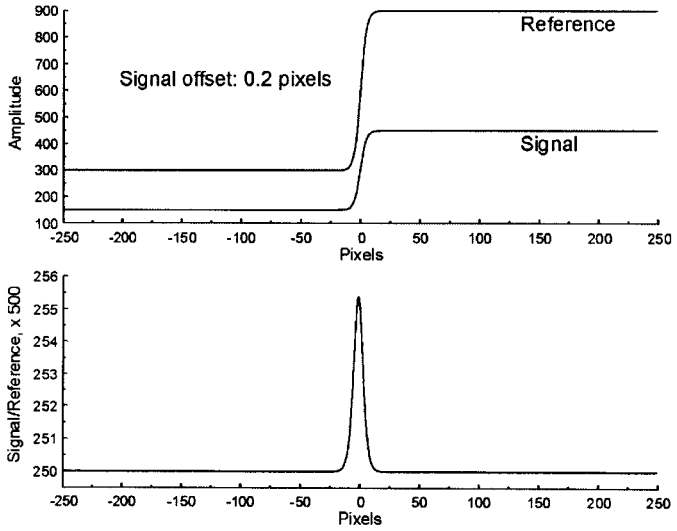

Figure 24.- Simulated misalignment of the signal image with the reference image to determine the effect on the normalized results.

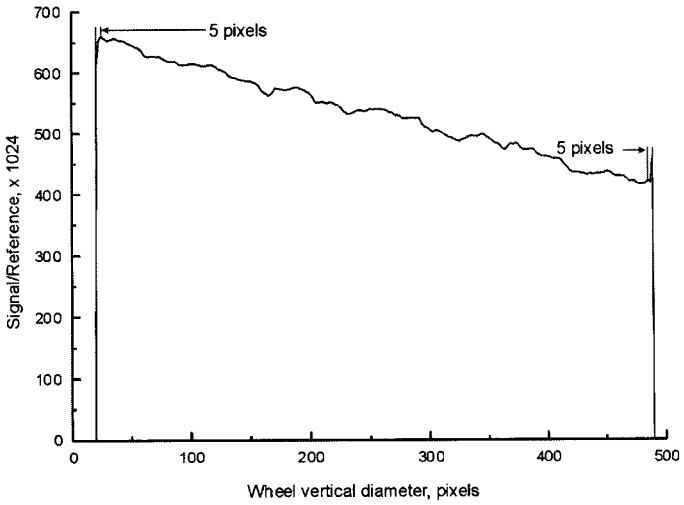

Figure 25.- Normalized signal amplitude along the vertical axis of a rotating wheel indicating a misalignment of the signal and reference images.

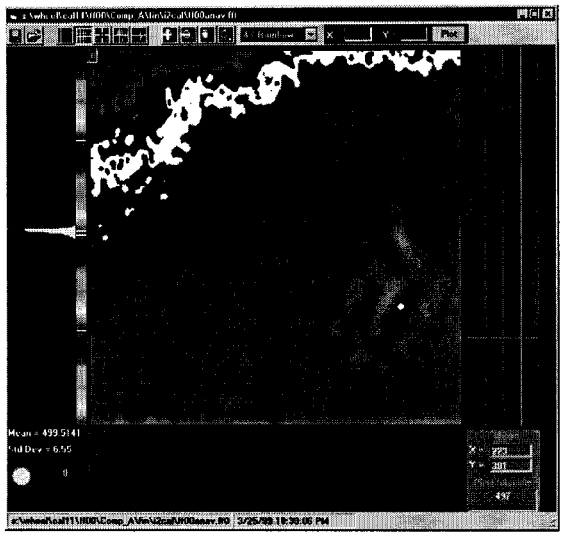

Figure 26.- Flat field calibration of the optical receiver system using the Iodine absorption line calibration target, (average of 50 images).

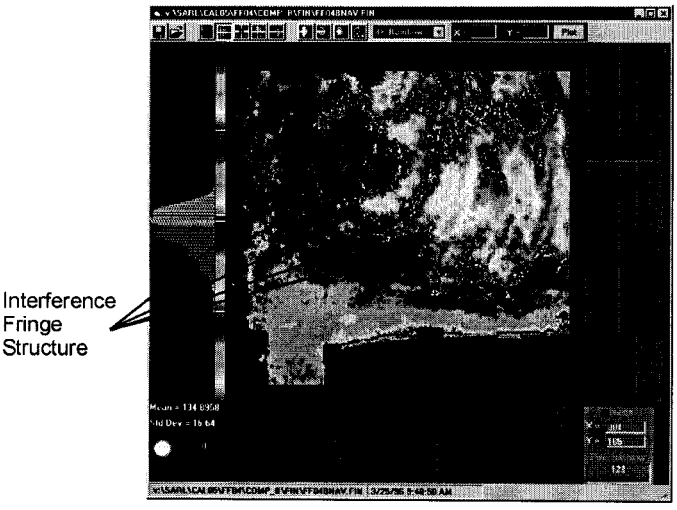

Figure 27.- Data image containing interference fringes caused by the Iodine vapor cell windows.

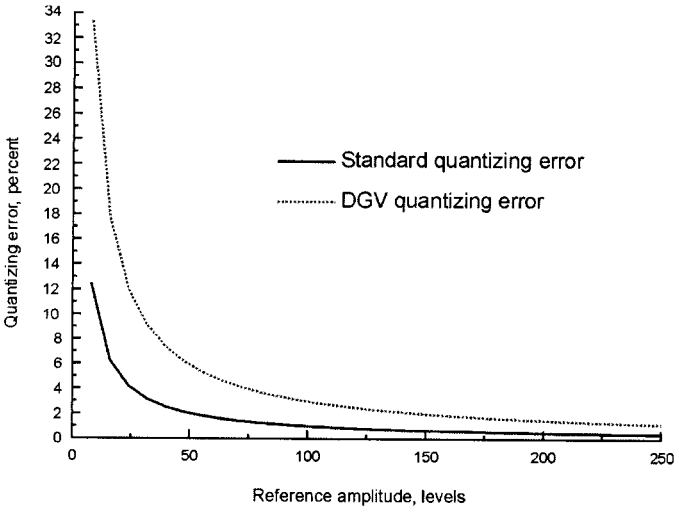

Figure 28.- Standard and DGV quantizing errors.

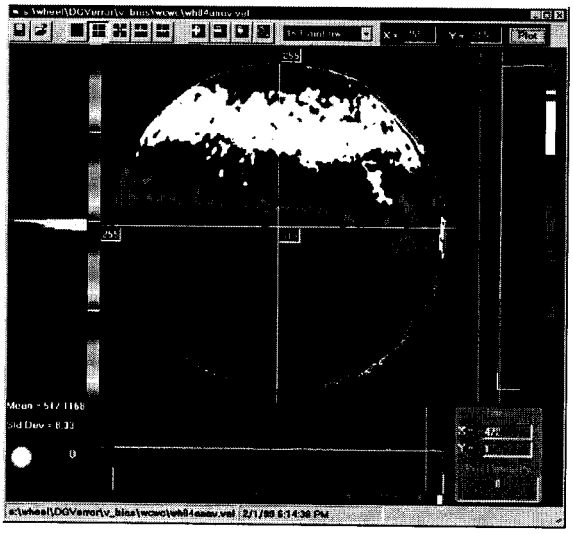

Figure 29.- Rotating wheel, horizontal velocity – Iodine absorption line calibration using the vellum target, Flat field obtained from the vellum target.

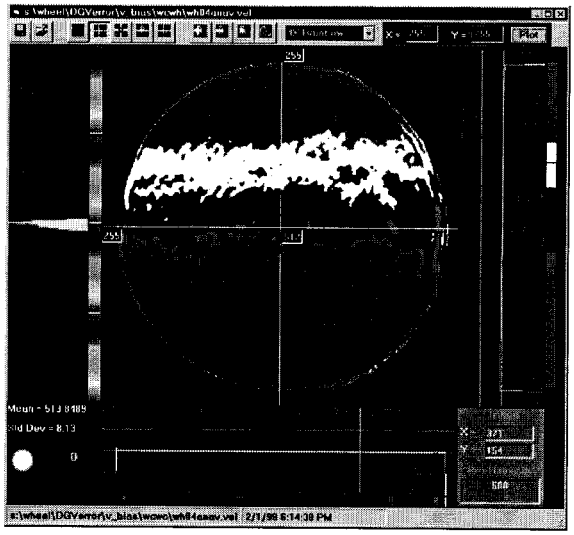

Figure 30.- Rotating wheel, horizontal velocity – Iodine absorption line calibration using the vellum target, Flat field obtained from the slowly rotating wheel.